

Dynamical mass ejection from the merger of asymmetric binary neutron stars: Radiation-hydrodynamics study in general relativity

Yuichiro Sekiguchi,¹ Kenta Kiuchi,² Koutarou Kyutoku,³ Masaru Shibata,² and Keisuke Taniguchi⁴

¹*Department of Physics, Toho University, Funabashi, Chiba 274-8510, Japan*

²*Yukawa Institute for Theoretical Physics, Kyoto University, Kyoto, 606-8502, Japan*

³*Interdisciplinary Theoretical Science (iTHES) Research Group, RIKEN, Wako, Saitama 351-0198, Japan*

⁴*Department of Physics, University of the Ryukyus, Nishihara, Okinawa 903-0213, Japan*

(Dated: September 17, 2018)

We perform neutrino radiation-hydrodynamics simulations for the merger of asymmetric binary neutron stars in numerical relativity. Neutron stars are modeled by soft and moderately stiff finite-temperature equations of state (EOS). We find that the properties of the dynamical ejecta such as the total mass, neutron richness profile, and specific entropy profile depend on the mass ratio of the binary systems for a given EOS in a unique manner. For the soft EOS (SFHo), the total ejecta mass depends weakly on the mass ratio, but the average of electron number per baryon (Y_e) and specific entropy (s) of the ejecta decreases significantly with the increase of the degree of mass asymmetry. For the stiff EOS (DD2), with the increase of the mass asymmetry degree, the total ejecta mass significantly increases while the average of Y_e and s moderately decreases. We find again that only for the soft EOS (SFHo), the total ejecta mass exceeds $0.01M_\odot$ irrespective of the mass ratio chosen in this paper. The ejecta have a variety of electron number per baryon with its average approximately between $Y_e \sim 0.2$ and ~ 0.3 irrespective of the EOS employed, which is well-suited for the production of the r-process heavy elements (second and third peaks), although its averaged value decreases with the increase of the degree of mass asymmetry.

PACS numbers: 04.25.D-, 04.30.-w, 04.40.Dg

I. INTRODUCTION

The merger of binary neutron stars is one of the most promising sources of gravitational waves for ground-based advanced detectors, such as advanced LIGO, advanced VIRGO, and KAGRA [1]. Among them, advanced LIGO already started the first observational run and has achieved the first direct detection of gravitational waves, which were emitted from a binary-black-hole merger [2]. We should expect that these gravitational-wave detectors will also detect the signals of gravitational waves from binary-neutron-star mergers in a few years, because the latest statistical studies suggest that these gravitational-wave detectors will observe gravitational waves from merger events as frequently as ~ 1 – $100/\text{yr}$ if the designed sensitivity is achieved [3–5].

Binary-neutron-star mergers are also attracting attention as one of the major nucleosynthesis sites of heavy elements produced by the rapid neutron capture process (r-process) [6], because a significant fraction of the neutron-rich matter is likely to be ejected during the merger (see Ref. [7] for the pioneering work). Associated with the production of the neutron-rich heavy elements in the matter ejected during the merger, a strong electromagnetic emission could be accompanied by the radioactive decay of the r-process heavy elements [8–10]. This will be an electromagnetic counterpart of gravitational waves from binary-neutron-star mergers and its detection could be used to verify the binary-neutron-star-merger scenario for the r-process nucleosynthesis. This hypothesis is encouraged in particular by the observation of an infrared transient event associated with a short-hard gamma-ray

burst, GRB 130603B [11]. These facts strongly encourage the community of gravitational-wave astronomy to theoretically explore the mass ejection mechanisms, the r-process nucleosynthesis in the ejecta, and associated electromagnetic emission in the mergers of binary neutron stars.

For the quantitative study of these topics, we have to clarify the merger process, subsequent mass ejection, physical condition of the ejecta, nucleosynthesis and subsequent decay of the heavy elements in the ejecta, and electromagnetic emission from the ejecta. For these issues, a numerical-relativity simulation, taking into account the detailed microphysical processes and neutrino radiation transfer, is the unique approach. In our previous paper [12], we reported our first numerical-relativity results for these issues focusing only on the equal-mass binaries. We found that the total mass of the dynamically ejected matter during the merger depends strongly on the equations of state (EOS) we employed, while the ejecta components have a wide variety of electron number per baryon (denoted by Y_e) between ≈ 0.05 and ≈ 0.5 irrespective of the EOS employed (see also Refs. [13–16]). The broad Y_e distribution is well-suited for explaining the abundance patterns for the r-process heavy elements with the mass number larger than ~ 90 in the solar system and ultra metal-poor stars [17].

In this article, we extend our previous study focusing on the merger of asymmetric binary neutron stars: We will report our latest numerical results for unequal-mass binary systems of typical neutron-star mass (between 1.25 and $1.45M_\odot$) for a soft (SFHo) EOS [18] and a moderately stiff (DD2) EOS [19]. We will show that

the physical properties of the merger ejecta depend on the degree of the mass asymmetry of the system: The ejecta mass varies with the mass ratio for a fixed value of the binary total mass, and the averaged value of Y_e decreases with the increase of the mass asymmetry degree, although Y_e is always broadly distributed irrespective of the mass ratio.

The paper is organized as follows. In Sec. II, we briefly review the formulation and numerical schemes employed in our numerical-relativity simulation, and also summarize the EOS we employ. In Sec. III, we present numerical results focusing on the dynamical mass ejection and properties of the merger remnants. Section IV is devoted to a summary. Throughout this paper, c and G denote the speed of light and the gravitational constant, respectively.

II. METHOD, EOS, INITIAL MODELS, AND GRID SETUP.

We solve Einstein's equation by a puncture-Baumgarte-Shapiro-Shibata-Nakamura formalism as before [12, 20, 21]. The fourth-order finite-differencing scheme is applied to discretize the field equations except for the advection terms for which the lop-sided scheme is employed. The radiation hydrodynamics equations are solved in the same manner as in Ref. [12]: Neutrino radiation transfer is computed in a leakage scheme [22] interpolating Thorne's moment formalism with a closure relation for a free-streaming component [23, 24]. For neutrino heating, which could induce a neutrino-driven wind from the merger remnant, absorption on free nucleons is taken into account.

We employ a soft (SFHo) [18] and a moderately stiff (DD2) [19] EOS for the nuclear-matter EOS, which have been derived recently by Hempel and his collaborators. For these EOS, the predicted maximum mass for spherical neutron stars is $2.06M_\odot$ and $2.42M_\odot$, respectively, and larger than the largest accurately-measured mass of neutron stars, $\approx 2.0M_\odot$ [25]. The radius of neutron stars with mass $1.35M_\odot$ for them is $R_{1.35} = 11.9$ km (SFHo EOS) and 13.2 km (DD2 EOS), respectively. These radii depend very weakly on the mass as long as it is in a typical neutron-star mass range between 1.2 and $1.5M_\odot$. Thus, we refer to an EOS with $R_{1.35} \leq 12$ km like SFHo EOS as soft EOS. The stellar radius plays a key role for determining the merger remnant and the properties of the dynamical ejecta as we already described in our previous paper [12].

In numerical simulations, we have to follow the ejecta with the typical velocity $0.2c$, which expand to $> 10^3$ km in ~ 20 ms. To follow the ejecta motion as well as to resolve neutron stars and merger remnants, we employ a fixed mesh-refinement algorithm. As in our previous work [12], we prepare 9 refinement levels with the varying grid spacing as $\Delta x_l = 2^{9-l}\Delta x_9$ ($l = 1, 2, \dots, 9$) and all the refinement levels have the same coordinate ori-

gin. Here, Δx_l is the grid spacing for the l -th level in Cartesian coordinates. For each level, the computational domain covers the region $[-N\Delta x_l, N\Delta x_l]$ for x - and y -directions, and $[0, N\Delta x_l]$ for z -direction (the reflection symmetry with respect to the orbital plane located at $z = 0$ is imposed). In the high-resolution run, we assign $N = 285$, $\Delta x_9 = 150$ m (for the SFHo EOS) or 160 m (for the DD2 EOS), and utilize $\approx 7,000$ CPUs on the K computer. Thus the location of outer boundaries along each axis is $L \gtrsim 10^4$ km and matter ejected from the central region never escape from the computational domain in our simulation time $\lesssim 60$ ms. To check whether the numerical results depend only weakly on the grid resolution, we also performed lower-resolution simulations for several models. For this case, $N = 160$ and $\Delta x_9 = 250$ m (for the SFHo EOS) or 270 m (for the DD2 EOS) and we confirm a reasonable convergence. We note that since good convergence is found for the models shown in Table I, we do not perform the low-resolution runs for all the models. In the following, the figures are plotted using the results by the high-resolution runs.

Choice of the floor density, which has to be put in a dilute-density or vacuum region outside the neutron stars and merger remnant when using the conservative form of hydrodynamics in numerical simulations, is one of the crucial artificial points for accurately exploring the mass ejection during the merger process. In this study, we set the floor density to be 1.67×10^4 g/cm³. The floor values of Y_e and temperature are 0.47 and 0.1 MeV, respectively. For this case, the artificial floor does not affect the quantitative results of the mass ejection for ~ 30 ms after the onset of the merger. In our experiments, we also performed simulations with the floor density 2×10^5 g/cm³. In this case, the inertia of the atmosphere is too high to follow the ejecta motion accurately: The effect of the atmosphere appeared on the ejecta at ~ 10 ms after the onset of the merger. In particular for the case that the ejecta mass is small ($\lesssim 10^{-3}M_\odot$), this artificial effect is serious: For example, the ejecta mass steeply decreases with time for such a low-mass ejecta case because the ejecta are decelerated significantly. We find that it is necessary to reduce the floor density much below 10^5 g/cm³ to follow the ejecta for sufficiently long time until the ejecta motion approximately relaxes to a free expansion stage ¹.

We consider binary neutron stars with each mass between $1.25M_\odot$ and $1.45M_\odot$ fixing the total mass to be $2.7M_\odot$. Neutron stars observed in *compact* binary systems typically have the mass ratio between 0.9 and 1.0, and each mass in the range 1.23 – $1.45M_\odot$ [26]. Thus,

¹ Our numerical results for the ejecta mass is much larger than those by Ref. [13] in which simulations are also performed using the SFHo and DD2 equations of state. We speculate that one of the reasons for this would be that our floor density is much smaller than that in Ref. [13] which employs 5×10^5 g/cm³. See Sec. III B for another reason.

TABLE I. The parameters and the results of the models employed in this study. m_1 and m_2 : each mass of binary in isolation. q : mass ratio defined by $m_2/m_1 (\leq 1)$. Δx_9 : the grid spacing in the finest refinement level. N : the grid number in one positive direction for each refinement level. M_{ej} , $\langle Y_e \rangle$, and V_{ej} denote the dynamical ejecta mass, the averaged value of Y_e , and ejecta velocity measured at 30 ms after the onset of the merger. M_{BH} and a_{BH} are the mass and dimensionless spin parameter of the remnant black holes, and M_{torus} is the mass of tori surrounding the remnant black holes for the SFHo models. These values are also measured at 30 ms after the onset of the merger. Model name follows the EOS, each mass m_2 and m_1 , and grid resolution. The equal-mass data are taken from Ref. [12].

Model	(m_1, m_2)	$q = m_2/m_1$	Δx_9 (m)	N	$M_{\text{ej}} (10^{-2} M_\odot)$	$\langle Y_e \rangle$	V_{ej}	$M_{\text{BH}} (M_\odot)$	a_{BH}	$M_{\text{torus}} (M_\odot)$
SFHo-135-135h (high)	(1.35, 1.35)	1.00	150	285	1.1	0.31	0.22	2.59	0.69	0.05
SFHo-135-135l (low)	(1.35, 1.35)	1.00	250	160	1.3	0.32	0.21	2.60	0.70	0.03
SFHo-133-137h (high)	(1.37, 1.33)	0.97	150	285	0.9	0.30	0.21	2.59	0.67	0.06
SFHo-130-140h (high)	(1.40, 1.30)	0.93	150	285	0.6	0.27	0.20	2.58	0.67	0.09
SFHo-130-140l (low)	(1.40, 1.30)	0.93	250	160	0.6	0.27	0.21	2.58	0.67	0.08
SFHo-125-145h (high)	(1.45, 1.25)	0.86	150	285	1.1	0.18	0.24	2.58	0.66	0.12
SFHo-125-145l (low)	(1.45, 1.25)	0.86	250	160	1.2	0.19	0.23	2.58	0.66	0.11
DD2-135-135h (high)	(1.35, 1.35)	1.00	160	285	0.2	0.30	0.16	–	–	–
DD2-135-135l (low)	(1.35, 1.35)	1.00	270	160	0.2	0.30	0.15	–	–	–
DD2-130-140h (high)	(1.40, 1.30)	0.93	160	285	0.3	0.26	0.18	–	–	–
DD2-125-145h (high)	(1.45, 1.25)	0.86	160	285	0.5	0.20	0.19	–	–	–

our choice reasonably reflects the observational fact. The initial orbital separation is chosen so that the orbital angular velocity, Ω , satisfies $Gm_0\Omega/c^3 = 0.028$ where m_0 denotes the total mass, i.e., $m_1 + m_2 = 2.7M_\odot$, and m_1 and $m_2 (\leq m_1)$ are the mass of each neutron star in isolation. Table I lists the key parameters of our models and simulation setup. We define the mass ratio by $q := m_2/m_1 (\leq 1)$.

III. NUMERICAL RESULTS

A. Summary of the merger process

For all the models we employ in our simulations, a massive neutron star (MNS) is first formed after the onset of the merger as expected from our previous results [12, 27] (see also our earlier papers [28]). The MNS are long-lived in the sense that their lifetime is much longer than their dynamical time scale and rotation period $\lesssim 1$ ms. The subsequent evolution of the MNS depends on the equations of state employed.

For the models with the SFHo EOS, the MNS with mass $\gtrsim 2.6M_\odot$ is hypermassive (see Refs. [29, 30] for the definition of the hypermassive neutron star) because the maximum mass of spherical and rigidly rotating cold neutron stars is only $\approx 2.06M_\odot$ and $\approx 2.45M_\odot$, respectively, which are smaller than the remnant MNS mass. As a result, the MNS collapses to a black hole at ~ 10 ms after the onset of the merger irrespective of the mass ratio after the angular momentum inside the MNS is redistributed by the gravitational torque associated with the non-axial symmetric matter distribution or is dissipated by the gravitational-wave emission.

The mass and dimensionless spin parameter of the

formed black holes are $\approx 2.6M_\odot$ and ~ 0.65 – 0.70 , respectively, and the remnant black holes are surrounded by a torus with mass ~ 0.05 – $0.1M_\odot$ and with their typical extent in the orbital plane ~ 100 km (see Table I and Sec. III C for more details). Such a compact torus would be subsequently evolved by a magneto-viscous process with the typical lifetime $\tau_v \sim (\alpha_v \Omega)^{-1}$ where α_v is the so-called α -parameter for viscous hydrodynamics and $\tau_v \sim 10^2 \text{ ms} (\alpha_v/10^{-2})^{-1}$ for $\Omega = O(10^3 \text{ rad/s})$ (see, e.g., Ref. [31]). Thus, for a plausible value of $\alpha_v \sim 0.01$, this system is a candidate for the central engine of short-hard gamma-ray bursts with the duration less than one second, like GRB 130603B [11] (see also Sec. III E).

For the DD2 case, any of the formed MNS does not collapse to a black hole in our simulation time ~ 50 ms. This is reasonable because the maximum mass of spherical and rigidly rotating cold neutron stars for the DD2 EOS is high, i.e., $\approx 2.42M_\odot$ and $2.8M_\odot$, respectively, and hence, the formed hot MNS with mass $\sim 2.6M_\odot$ are not hypermassive and cannot collapse to a black hole before a substantial fraction of the angular momentum and thermal energy are dissipated or carried away, respectively, by some angular-momentum transport processes and the neutrino emission (for which the cooling time scale is longer than 1 s; e.g., Refs. [21, 27]). The hot remnant MNS would be long-lived with their lifetime longer than a few seconds and could be a strong emitter of neutrinos, which can modify the chemical property of the ejecta via the neutrino irradiation process (see Sec. III C).

B. Dynamical mass ejection

Figure 1 plots the evolution of the total rest mass, M_{ej} , and the averaged value for the electron number per

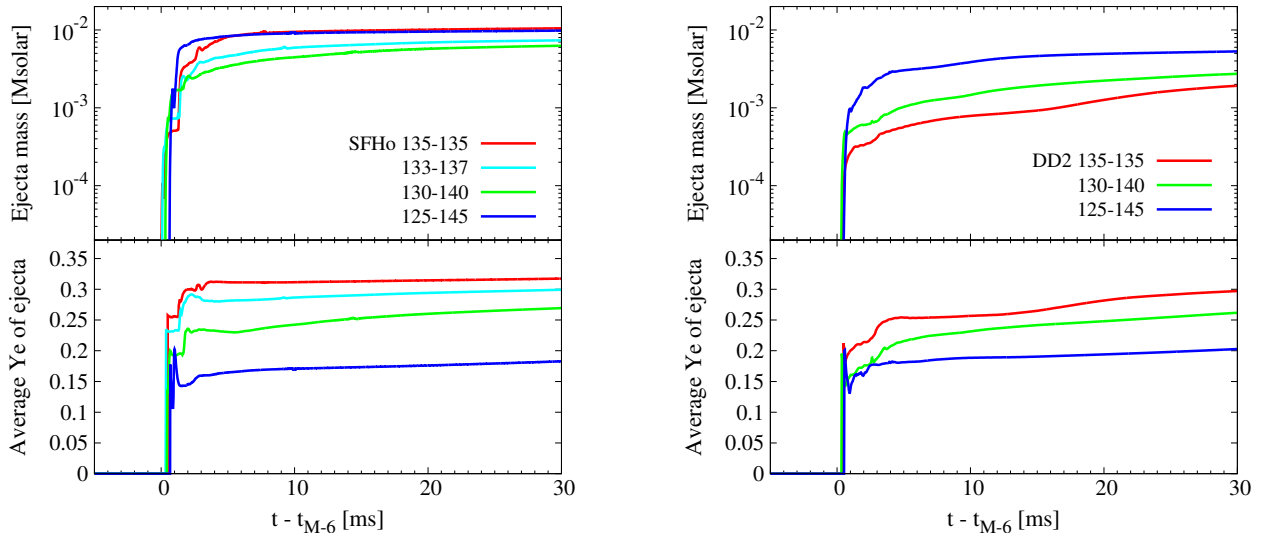


FIG. 1. Rest mass (upper panel) and averaged value of Y_e (lower panel) of the dynamical ejecta as functions of time for the SFHo (left) and DD2 (right) models and for a variety of binary mass ratios. t_{M-6} approximately denotes the time at the onset of the merger (see text). The results for the high-resolution runs are plotted. A substantial fraction of the matter is dynamically ejected at $t - t_{M-6} \gtrsim 2$ ms but gradual ejection continues subsequently. The long-term gradual increase of the ejecta mass and the averaged value of Y_e for $t_{M-6} \gtrsim 10$ ms, observed in particular for the DD2 case, is due to the irradiation by neutrons that are emitted from the merger remnant.

baryon, $\langle Y_e \rangle$, of the ejecta for the models with the SFHo and DD2 EOS for a variety of mass ratios. Here, t_{M-6} approximately denotes the time at the onset of the merger: It denotes the time at which M_{ej} exceeds $10^{-6} M_{\odot}$. The average of Y_e for the ejecta is defined by

$$\langle Y_e \rangle = \frac{1}{M_{\text{ej}}} \int Y_e dM_{\text{ej}}. \quad (3.1)$$

We specify the matter as the ejecta if the lower time component of the fluid four velocity, u_t , is smaller than -1 as before [12]. We note that this condition agrees approximately with the condition $hu_t < -1$ where h is the specific enthalpy. The reason for this is that h is close to unity for the ejecta components moving far from the merger remnant located in the central region. In Table I, we also summarize the total rest mass, the averaged value of Y_e , and the averaged velocity of the ejecta, V_{ej} , all of which are measured at $t - t_{M-6} \approx 30$ ms. Here, V_{ej} is defined by $\sqrt{2E_{\text{kin}}/M_{\text{ej}}}$ where E_{kin} is total kinetic energy of the ejecta.

Figure 1 illustrates that the ejecta mass depends strongly on the EOS employed, as already described in Ref. [12]: For the smaller value of $R_{1.35}$, the ejecta mass is larger (see also Ref. [13]). Figure 1 also shows that for the models with the SFHo EOS, the ejecta mass depends weakly on the binary mass asymmetry, while for those with the DD2 EOS, it increases steeply with the increase of the degree of the binary mass asymmetry. As already described in our study of Ref. [32] in which piecewise polytropic EOS is employed, this is due to the fact that

there are two major dynamical mass ejection mechanisms (see also Ref. [33]): shock heating and tidal interaction (i.e., tidal torque exerted by elongated two neutron stars and highly non-axisymmetric merger remnants). For the equal-mass or slightly asymmetric case, the shock heating is the primary player of the dynamical mass ejection for neutron stars with soft EOS like the SFHo EOS, while the tidal torque is the primary player for binary neutron stars with stiff EOS like the DD2 EOS.

The shock heating efficiency during the merger phase decreases with the increase of the binary asymmetry degree because the smaller-mass neutron star in such asymmetric systems is tidally elongated just prior to the onset of the merger, avoiding the coherent collision with the heavier companion at the merger. Thus, for the models with the SFHo EOS, the shock heating effect is weakened with the increase of the binary asymmetry degree while the importance of the tidal effect is enhanced. As a result of this change in the dynamical mass ejection mechanism, the ejecta mass slightly decreases with the change of q from unity to a smaller value to ~ 0.9 . However, with the further decrease of q (i.e., with the further increase of the degree of the mass asymmetry), the ejecta mass increases because the enhanced tidal effect dominates the reduced shock heating effect.

On the other hand, for the DD2 models the tidal interaction is always the primary mechanism for the dynamical mass ejection. The importance of the tidal effect is further enhanced with the increase of the mass asymmetry degree for this EOS, monotonically increasing the dynamical ejecta mass. Thus, for significantly asymmetric

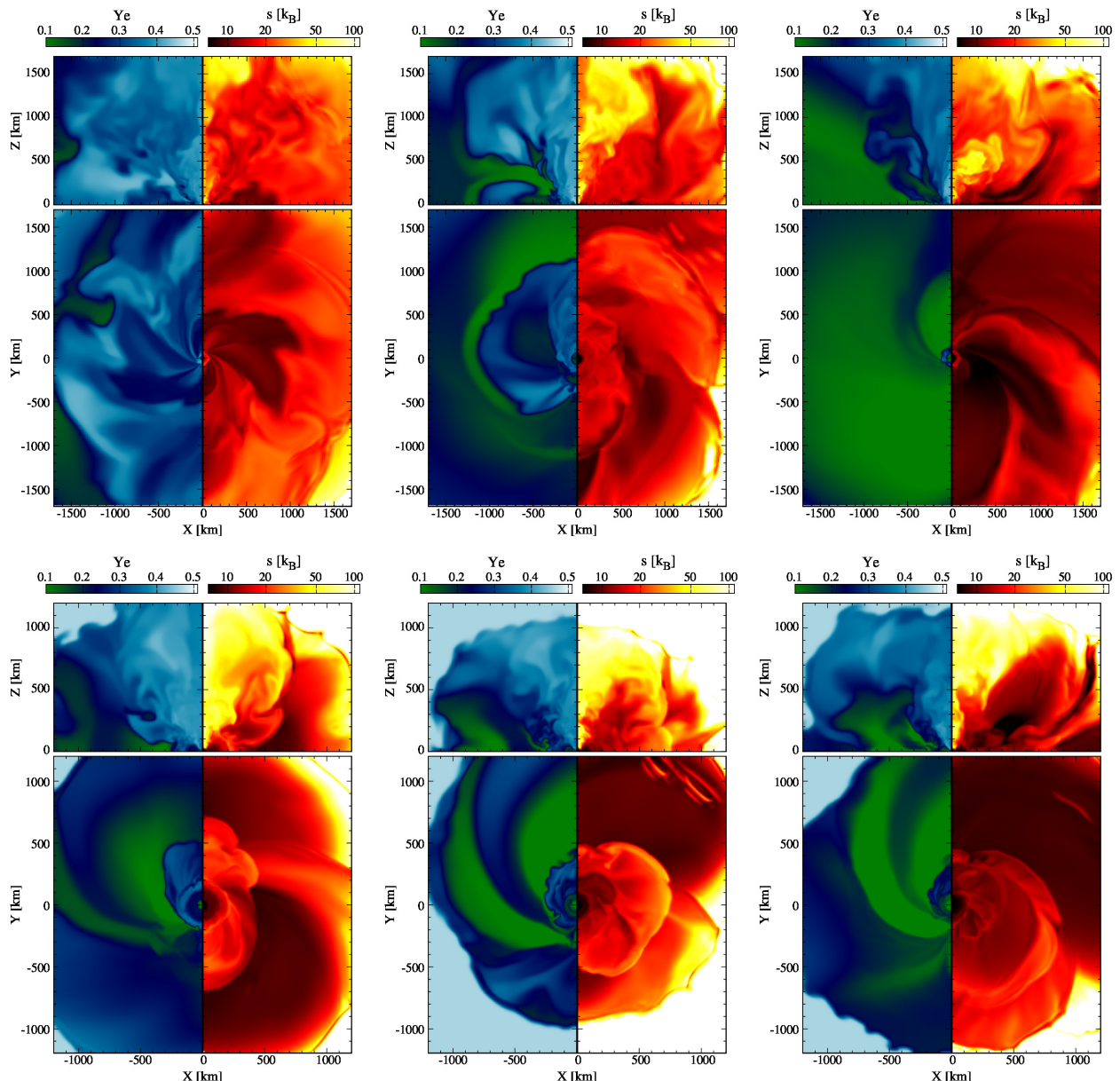


FIG. 2. Profiles of the electron number per baryon, Y_e , (left in each panel) and the specific entropy, s , (right in each panel) in $x-y$ (lower in each panel) and $x-z$ (upper in each panel) planes. The top three panels show the results for SFHo-135-135h (left), SFHo-130-140h (middle), and SFHo-125-145h (right) at ≈ 13 ms after the onset of the merger. The lower three panels show the results for DD2-135-135h (left), DD2-130-140h (middle), and DD2-125-145h (right) at ≈ 10 ms after the onset of the merger.

binaries, the typical ejecta mass would approach $10^{-2} M_{\odot}$ irrespective of the EOS employed. We note that the total ejecta mass depends only weakly on the grid resolution as listed in Table I.

As shown in Fig. 1, the ejecta mass increases with time for the first ~ 10 ms after the onset of the merger. This is in particular observed for the SFHo models with $q \gtrsim 0.9$ and all the DD2 models. This indicates that we have to follow the ejecta motion at least for ≈ 10 ms after the onset of the merger. In a recent simulation of Ref. [13],

they estimated the properties of the ejecta at $\lesssim 5$ ms after the onset of the merger, perhaps because of their small computational domain employed ($L = 750$ km). However, the ejecta mass would still increase with time in such an early phase. This could be one of the reasons that our results for the ejecta mass are much larger than theirs. Figure 1 also shows that the average of Y_e still significantly varies with time for the first ~ 5 ms after the onset of the merger. This also shows that it would be necessary to determine the properties of the ejecta at

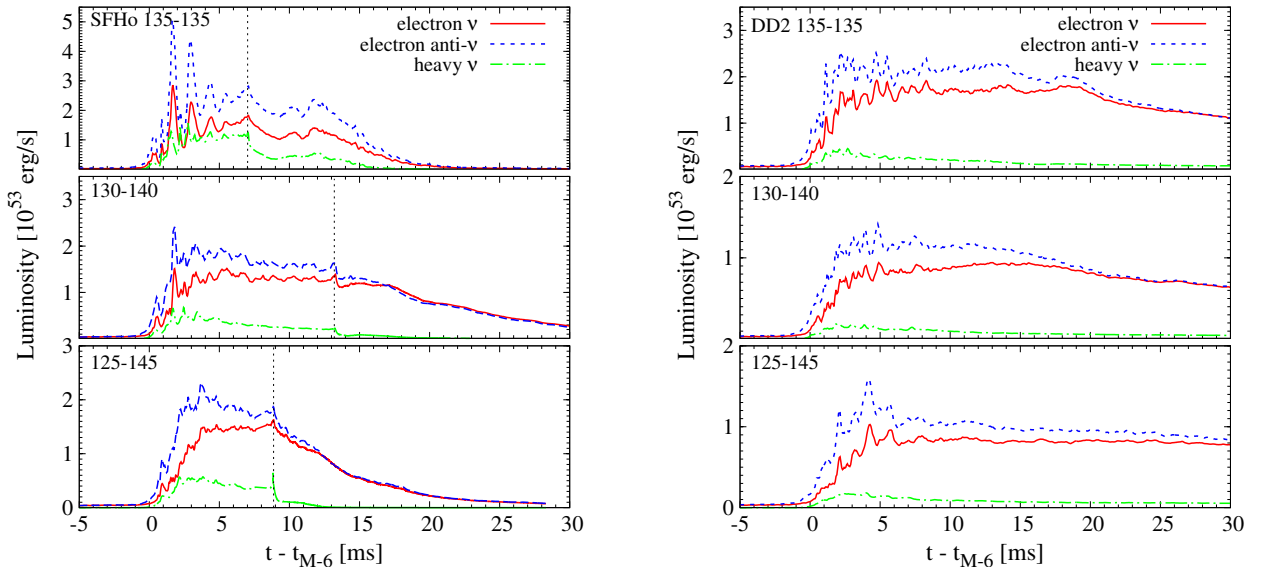


FIG. 3. Luminosity curves of ν_e (red solid), $\bar{\nu}_e$ (blue dashed), and heavy (green dotted-dashed) neutrinos for the models with the SFHo EOS (left) and the DD2 EOS (right), respectively (note that the scales in the vertical axis are different among the plots). For heavy neutrinos, the contribution from only one heavy species is plotted. The vertical dashed lines in the left panel shows the time at the formation of a remnant black hole. We note that the relatively high heavy-neutrino luminosity for the SFHo models before the collapse to the remnant black holes reflects the fact that the temperature of remnant MNS is higher and the pair-process neutrino emission is more active than those for the DD2 model.

$\gtrsim 10$ ms after the onset of the merger (if the average of Y_e is estimated at ~ 5 ms after the onset of the merger as in Ref. [13], the average of Y_e could be underestimated).

Irrespective of the EOS and mass ratios, the averaged ejecta velocity is in the range between $0.15c$ and $0.25c$, as found in Refs. [12, 16, 32]. As we already pointed out in Ref. [32], the ejecta velocity is higher for softer EOS and this shows that the shock heating effect enhances the ejecta velocity. On the other hand, the ejecta velocity depends only weakly on the mass ratio (as long as it is in the range $0.85 < q \leq 1$), although it is slightly increased for significantly asymmetric binaries like $1.25\text{--}1.45M_\odot$ models.

As described earlier in this section, shock heating and tidal interaction are two major dynamical mass ejection mechanisms. By the tidal torque, the matter tends to be ejected near the orbital plane because the tidal-force vector primarily points to the direction in this plane. On the other hand, by the shock heating, the matter is ejected in a quasi-spherical manner like in supernova explosion. Because both effects play a role, the dynamical ejecta usually have a spheroidal morphology [32].

For the SFHo models, the shock heating plays a primary role for the equal-mass or slightly asymmetric case, and hence, the dynamical ejecta in this case have a quasi-spherical morphology. However, for the significantly asymmetric case, e.g., with $q \sim 0.85$, the tidal effect becomes appreciable, as already mentioned, and hence, the anisotropy of the dynamical ejecta is enhanced. On the other hand, for the DD2 models, the tidal torque always plays a primary role for the dynamical mass ejection.

Thus, with the increase of the binary asymmetry degree, this property is further enhanced, and the anisotropy of the dynamical ejecta morphology is increased. Here, we note that the degree of the anisotropy is correlated with the neutron-richness of the dynamical ejecta because (i) the tidally ejected components are less subject to the thermal weak-interaction reprocess associated with the shock heating preserving the neutron-rich nature of the original neutron-star matter and (ii) the neutrino irradiation is less subject to the matter near the equatorial plane than that near the polar region (see the discussion in Sec. III C).

Six panels of Fig. 2 display the profiles of the electron number per baryon, Y_e , (left side of each panel) and specific entropy, s , (right side of each panel) of the ejecta on the x - y and x - z planes for the SFHo (top panels) and DD2 (lower panels) models. For the SFHo and DD2 models, the snapshots at $t - t_{M-6} \approx 13$ ms and 10 ms are plotted, respectively. The left, middle, and right panels display the results for $1.35\text{--}1.35M_\odot$, $1.30\text{--}1.40M_\odot$, and $1.25\text{--}1.45M_\odot$, respectively. This figure shows a clear dependence of the properties of the dynamical ejecta on the binary asymmetry degree and on the EOS employed as follows:

(I) For the SFHo models, the specific entropy of the ejecta decreases steeply with the increase of the binary asymmetry degree in particular near the orbital plane. This is due to the fact that the effect of the shock heating at the onset of the merger, which contributes a lot to the dynamical mass ejection, becomes weak with the increase of the binary asymmetry degree.

(II) As a result, for the SFHo models, the ejecta component with low values of Y_e increases with the increase of the binary asymmetry degree: For the equal-mass case, the ejecta with $Y_e \gtrsim 0.2$ are the primary components while for the $1.25\text{--}1.45M_\odot$ model, those with $Y_e \lesssim 0.2$ are primary (in particular for the components near the orbital plane). This is due to the following fact: For a high temperature environment, e^-e^+ pair-creation is enhanced, and consequently, the positron capture reaction, $n + e^+ \rightarrow p + \bar{\nu}_e$, efficiently proceeds in neutron-rich matter, resulting in the increase of Y_e . With the increase of the binary asymmetry degree, the shock heating effect becomes less important and the temperature for a substantial fraction of the dynamical ejecta is decreased. As a result, the positron production and resulting positron capture are suppressed. Hence, the neutron richness is preserved to be relatively high (the value of Y_e is preserved to be low).

(III) For the DD2 models, the effect associated with the binary asymmetry found for the SFHo model is not very remarkable: The typical values of Y_e and specific entropy depend mildly on the binary asymmetry degree, although we still observe a monotonic decrease of these values (see, e.g., Fig. 1). This weak dependence is due to the fact that the ejecta are composed primarily of tidally-ejected matter irrespective of the mass ratio, as already mentioned.

C. Neutrino irradiation

For the DD2 models, the remnant massive neutron stars are long-lived, while for the SFHo models, the remnants collapse to a black hole in ~ 10 ms after the onset of the merger. Therefore, a high-luminosity neutrino emission is continued for a long time scale from the remnant of the DD2 models, while the strong emission continues only briefly for the SFHo models (see Fig. 3). As a result, a long-term *neutrino-irradiation* effect [12, 34, 36–38] plays an important role for heating up the ejecta and for increasing the value of Y_e (see Fig. 1), in particular in the region above the remnant MNS pole (see Fig. 2) in the DD2 model.

As we pointed out in Ref. [12], the reason for the increase of Y_e by the neutrino irradiation is as follows: The luminosity of electron neutrinos emitted from the remnant hot MNS is quite high as shown in Fig. 3. In such an environment, neutrino capture processes, $n + \nu_e \rightarrow p + e^-$ and $p + \bar{\nu}_e \rightarrow n + e^+$, are activated in the matter surrounding the MNS. By the balance of these reactions, the fractions of neutrons and protons are determined and the equilibrium value of Y_e will be given by (e.g., Ref. [39]),

$$Y_{e,\text{eq}} \sim \left[1 + \frac{L_{\bar{\nu}_e}}{L_{\nu_e}} \cdot \frac{\langle \epsilon_{\bar{\nu}_e} \rangle - 2\Delta}{\langle \epsilon_{\nu_e} \rangle + 2\Delta} \right]^{-1}, \quad (3.2)$$

where $\Delta = m_n c^2 - m_p c^2 \approx 1.293$ MeV, $\langle \epsilon_{\nu_e} \rangle$ and $\langle \epsilon_{\bar{\nu}_e} \rangle$ denote averaged neutrino energy of ν_e and $\bar{\nu}_e$, and L_{ν_e} and $L_{\bar{\nu}_e}$ denote the luminosity of ν_e and $\bar{\nu}_e$, respectively.

For the DD2 models, $\langle \epsilon_{\nu_e} \rangle \approx 10$ MeV, $\langle \epsilon_{\bar{\nu}_e} \rangle \approx 15$ MeV, and $L_{\bar{\nu}_e}/L_{\nu_e} \approx 1.0\text{--}1.3$, and consequently, the equilibrium value is $Y_e \approx 0.45\text{--}0.5$. Due to the neutrino irradiation, the neutron richness of the originally neutron-rich matter with $Y_e \lesssim 0.1$ is decreased (the average of Y_e is increased) towards the equilibrium value.

However, this neutrino irradiation effect depends on the binary asymmetry because, as Fig. 3 shows, the neutrino luminosity decreases with the increase of the binary asymmetry degree (this is in particular seen clearly among the DD2 models). A time scale for the increase of the average Y_e may be estimated approximately as

$$\begin{aligned} \tau_{Y_e} &\sim \langle Y_e \rangle \left[\frac{1}{4\pi r^2} \left(\frac{X_n \sigma_{\nu_e n} L_{\nu_e}}{\langle \epsilon_{\nu_e} \rangle} - \frac{X_p \sigma_{\bar{\nu}_e p} L_{\bar{\nu}_e}}{\langle \epsilon_{\bar{\nu}_e} \rangle} \right) \right]^{-1} \\ &\sim 40 \text{ ms} \left(\frac{L_\nu}{10^{53} \text{ ergs/s}} \right)^{-1} \left(\frac{r}{100 \text{ km}} \right)^2, \end{aligned} \quad (3.3)$$

where r is the coordinate radius, $\sigma_{\nu_e n}$ and $\sigma_{\bar{\nu}_e p}$ are the cross-sections of the ν_e absorption on neutrons and $\bar{\nu}_e$ on protons, respectively. Here, we set $\langle \epsilon_{\nu_e} \rangle = 10$ MeV, $\langle \epsilon_{\bar{\nu}_e} \rangle = 15$ MeV, $L_{\nu_e} = L_{\bar{\nu}_e} = L_\nu$, $X_n = 1 - \langle Y_e \rangle$, and $X_p = \langle Y_e \rangle$ with $\langle Y_e \rangle = 0.2$. Thus, for the asymmetric binaries for which L_ν is smaller than that for the equal-mass binary, the time scale to increase Y_e by the neutrino irradiation is longer, as found in Fig. 1: It shows that the rate for the long-term increase in $\langle Y_e \rangle$ is smaller for the more asymmetric binary models.

By this neutrino irradiation, the ejecta mass is also increased (see Fig. 1). This is in particular the case for the DD2 models with the equal-mass or weakly asymmetric systems, for which the remnant MNS is long-lived and a long-term increase of the ejecta component is observed. For the SFHo models, the MNS is hypermassive and collapses to a black hole in ~ 10 ms after the onset of the merger, reducing the neutrino luminosity. Thus, the effect of the neutrino irradiation is less important irrespective of the binary asymmetry degree.

D. Mass distribution of Y_e

The effect of the binary asymmetry is also reflected in the mass distribution of Y_e in an appreciable manner in particular for the SFHo models. Figure 4 shows histograms for the ejecta mass fraction as a function of Y_e at $t - t_{M-6} \approx 25$ ms, at which the total (dynamical) ejecta mass and the averaged value of Y_e approximately settle to relaxed values.

For the equal-mass or slightly asymmetric cases with the SFHo EOS, the ejecta typically have high values of the specific entropy due to strong shock heating at the onset of the merger (see Fig. 2). As a result of this high value (i.e., the high value of temperature), e^-e^+ pair-creation is enhanced and subsequently positron capture, $n + e^+ \rightarrow p + \bar{\nu}_e$, efficiently proceeds, resulting in the increase of $\langle Y_e \rangle$. Because the shock heating effect for the SFHo models is more significant than that for the DD2

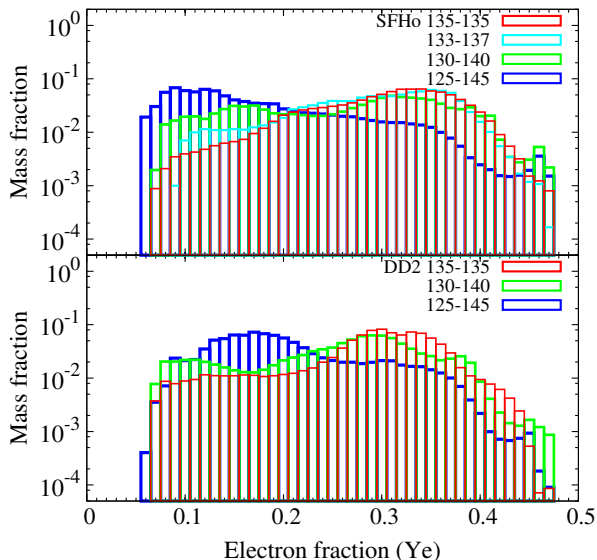


FIG. 4. The mass-distribution histograms with respect to Y_e normalized by the total mass of ejecta for the models with the SFHo EOS (top panel) and the DD2 EOS (lower panel), respectively. The data at $t - t_{M-6} \approx 25$ ms are employed.

models, the averaged value of Y_e for the ejecta of the SFHo models is higher than that of the DD2 models for the equal-mass or slightly asymmetric cases (see Fig. 1).

On the other hand, in the presence of appreciable binary asymmetry, not only the shock heating but also the tidal effect become important in the dynamical mass ejection even for the SFHo models. As a result, the fraction of matter with low values of Y_e is increased. This is clearly observed in Fig. 4, which shows that the value of Y_e at the peak gradually shifts to the lower-value side and in particular for the $1.25\text{--}1.45M_\odot$ model, the peak Y_e value is smaller than 0.2 both for the SFHo and DD2 models. However, even in such appreciably asymmetric cases, the dynamical ejecta have a broad distribution in Y_e . This is the universal qualitative feature and well-suited for producing a variety of r -process heavy elements [17].

E. Properties of the merger remnant

We briefly touch on the properties of the merger remnants located around the central region because the torus around the central merger remnant could be the origin of the further long-term mass ejection (e.g., Refs. [35–37]). For the SFHo models, the outcome for $t - t_{M-6} \gtrsim 15$ ms is a rotating black hole surrounded by a massive torus irrespective of the mass ratio, as displayed in Fig. 5. For the SFHo-135-135 model, the torus mass is $\approx 0.05M_\odot$ and its maximum density is less than 10^{12} g/cm³. For such relatively low density, the electron degeneracy is not very

high and also neutrinos escape efficiently from the torus because the optical depth is small.

On the other hand, for the SFHo-125-145 model (also for the SFHo-130-140 model), the torus mass and maximum density are higher than those for the SFHo-135-135 model. In this case the maximum density is higher than $\sim 10^{12}$ g/cm³, the electron degeneracy is higher than that for the SFHo-135-135 model, and a part of neutrinos is trapped. Then, the β -equilibrium among neutrons, protons, electron, and neutrinos as $n + \nu_e \leftrightarrow p + e^-$ and $p + \bar{\nu}_e \leftrightarrow n + e^+$ is approximately satisfied. Since the electron degeneracy is high, the resulting value of Y_e is lower than that for the SFHo-135-135 model.

Irrespective of the binary mass asymmetry, the resulting compact torus has high temperature ~ 10 MeV and is cooled dominantly by the neutrino emission. Hence the torus is the neutrino-dominated accretion torus. The order of magnitude for the neutrino luminosity (for ν_e and $\bar{\nu}_e$) is 10^{52} ergs/s (see Fig. 3). Thus, the pair annihilation of neutrinos and anti-neutrinos to the electron-positron pair, which is not taken into account in our present simulation, would be activated and could modify the dynamics of the merger remnants (e.g., Refs. [40, 41]). In addition, the system has a low density region above the black-hole pole. Such a system satisfies the conditions for the central engine of short-hard gamma-ray bursts.

Massive tori will be subsequently evolved by magnetohydrodynamics (MHD) or viscous processes in reality: Angular momentum inside the tori will be redistributed and associated with this effect, matter in the tori will be heated up. Then, the geometrical thickness of the tori will be increased, and possibly, an outflow that ejects the matter from the outer part of the tori could be launched [31, 35–38]. The total rest mass of the ejected matter could reach 10% of the initial torus mass, according to the previous studies. This suggests that the ejecta with mass of the order $0.01M_\odot$ could follow the dynamical mass ejection. We need to explore this process in our future study. On the other hand, the luminosity of neutrinos emitted is not as high as that by the remnant MNS. Thus, neutrino irradiation would not be as important as the MHD/viscous effect for the mass ejection in the black hole-torus system.

For the DD2 models, the final outcome is a MNS surrounded by a massive torus as displayed in Fig. 5. Although the central object is different from a black hole, the surrounding matter distribution and velocity profile (close to the Keplerian motion) are similar to those for the SFHo models. Because the density of the MNS and torus is higher than the torus surrounding the black hole found in the SFHo models, the low value of Y_e caused by the electron degeneracy is clearly observed in the DD2 models. As in the torus surrounding black holes, the torus around the MNS would be subject to the MHD or viscous effects [38], and hence, it is natural to expect a substantial fraction of mass ejection from the surrounding matter. Because the MNS is long-lived for the DD2 models, it is also natural to expect that the neutrino ir-

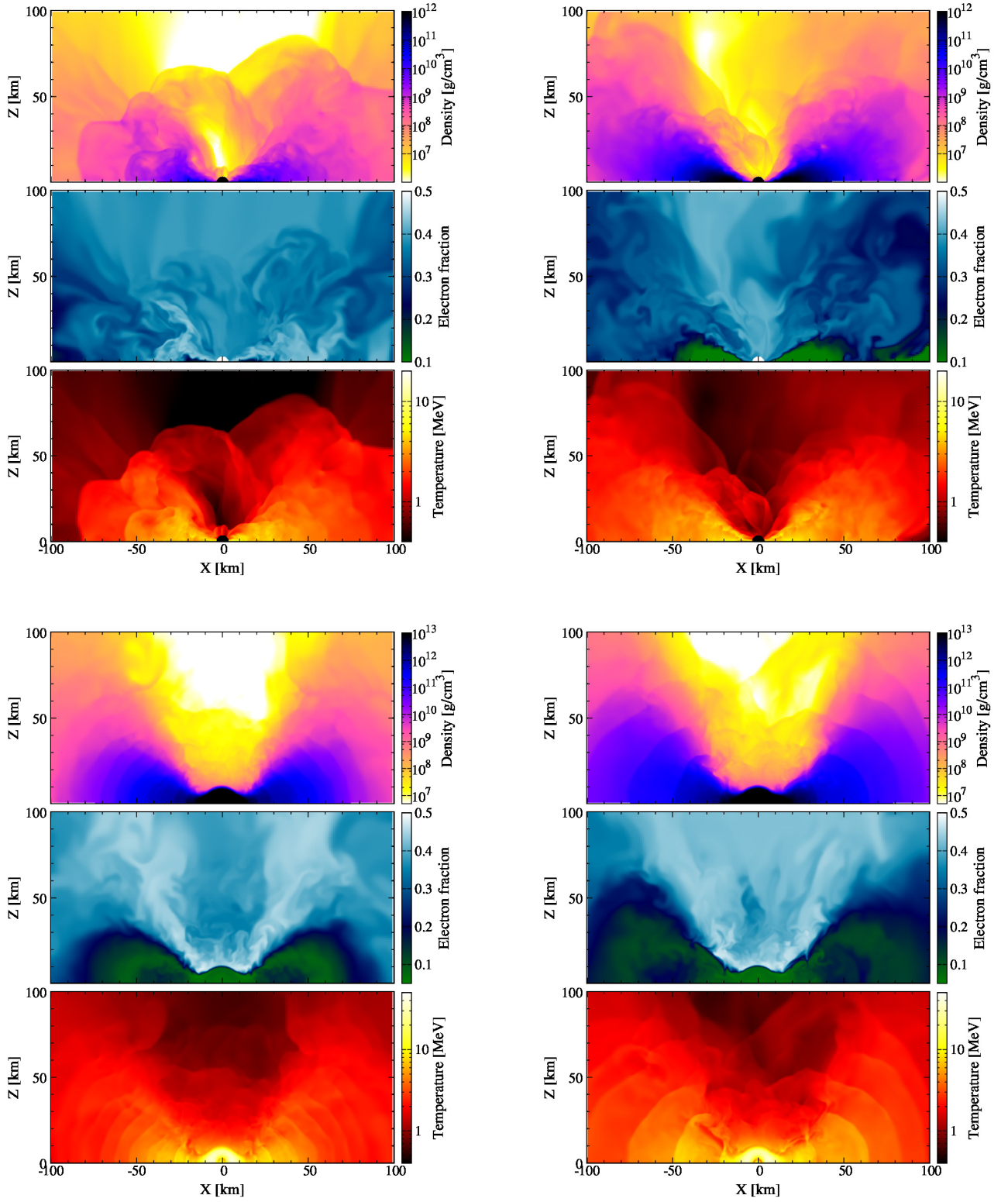


FIG. 5. Profiles of the rest-mass density (top in each panel), electron number per baryon (middle in each panel), and temperature (bottom in each panel) in x - z plane for SFHo-135-135h (top left), SFHo-125-145h (top right), DD2-135-135h (bottom left), and DD2-125-145h (bottom right) at 30 ms after the onset of the merger. The filled circles (in black or white) in the top panels denote the inside of black holes.

radiation to the surrounding matter plays an important role for inducing long-term mass ejection.

In the DD2 models, the torus mass and torus extent for the asymmetric binaries are larger than that for the equal-mass one as in the SFHo models. This shows that the binary asymmetry increases not only the dynamical ejecta mass but also the torus mass. This suggests that the mass of the matter ejected by subsequent MHD/viscous effect would be also enhanced in the asymmetric models.

The outer part of the torus surrounding the central object, that is most subject to the mass ejection from the torus, is in general hot and the value of Y_e is not very small ($\gtrsim 0.35$). This suggests that the ejecta would not be very neutron-rich and less subject to producing the heavy r-process elements, although they could be subject to producing relatively light r-process elements. Exploring the torus-originated components of the ejecta in a self-consistent study from the merger simulation throughout the subsequent remnant evolution will be an important issue to fully understand the mass ejection mechanism in the binary-neutron-star merger event. We plan to explore this issue in our future work.

It is interesting to point out that for the DD2 models, the density in the region above the MNS pole is as low as $\lesssim 10^7 \text{ g/cm}^3$ for $t - t_{M-6} \gtrsim 20 \text{ ms}$. Since the luminosity of electron neutrinos and anti-neutrinos emitted from the remnant MNS is high, $\sim 10^{53} \text{ ergs/s}$, for the DD2 models, the $\nu_e \bar{\nu}_e$ pair annihilation would be active near the MNS. According to a simple order of magnitude estimate, the pair annihilation luminosity is given by (e.g., Refs. [40, 42])

$$\begin{aligned}
 L_{\nu_e \bar{\nu}_e} &\sim 10^{50} \text{ ergs/s} \left(\frac{r}{10^7 \text{ cm}} \right)^{-1} \left(\frac{\langle \epsilon_{\nu_e} \rangle + \langle \epsilon_{\bar{\nu}_e} \rangle}{20 \text{ MeV}} \right) \\
 &\times \left(\frac{L_{\nu_e}}{10^{53} \text{ ergs/s}} \right) \left(\frac{L_{\bar{\nu}_e}}{10^{53} \text{ ergs/s}} \right) \\
 &\times \left(\frac{\cos \Theta}{0.1} \right)^2 \left(\frac{\theta_{\text{open}}}{0.1} \right)^{-2}, \quad (3.4)
 \end{aligned}$$

where Θ is the typical angle of the collision between ν_e and $\bar{\nu}_e$, r and θ_{open} denote, respectively, the extent and opening angle above the MNS pole, in which the pair annihilation is enhanced. This luminosity is high enough for launching short-hard gamma-ray bursts like GRB 130603B even for the case that the merger remnant is surrounded by dynamical ejecta, as demonstrated in Ref. [43]. Because the density of the polar region in the vicinity of the MNS is low, high specific entropy would be achieved in the presence of the $\nu_e \bar{\nu}_e$ pair annihilation. This suggests that a strong outflow or a jet may be launched from this system. If a sufficiently high specific entropy is achieved, a relativistic jet responsible for a short-hard gamma-ray burst could be indeed launched even from the remnant MNS. Including the $\nu_e \bar{\nu}_e$ pair annihilation in our simulation will be an important next step.

IV. SUMMARY AND DISCUSSION

We have reported our latest numerical results of neutrino radiation hydrodynamics simulations for binary-neutron-star mergers in general relativity, focusing on the dynamical mass ejection from the merger of asymmetric binary neutron stars with typical mass for each neutron star ($1.25\text{--}1.45M_\odot$) and with two representative finite-temperature EOS. The following is the summary of our finding:

1. The dynamical ejecta mass depends weakly on the mass ratio for the SFHo (soft-EOS) models. The reason for this is that while the dynamical mass ejection from equal-mass or nearly equal-mass system is induced primarily by shock heating and this effect becomes weak with the increase of the degree of the binary asymmetry, the tidal effect compensates the weakened shock-heating effect for the mass ejection in the asymmetric systems.
2. The dynamical ejecta mass depends significantly on the binary asymmetry degree for the DD2 (moderately stiff-EOS) models; it is $\approx 2 \times 10^{-3} M_\odot$ for the equal-mass case while it is $\approx 5 \times 10^{-3} M_\odot$ for the $1.25\text{--}1.45M_\odot$ model. The reason for this is that the tidal torque, which plays a major role for the dynamical mass ejection in this EOS, is simply enhanced.
3. The averaged value of Y_e decreases appreciably with the increase of the degree of the binary asymmetry irrespective of the EOS employed, and the peak value of Y_e becomes less than 0.2 for the $1.25\text{--}1.45M_\odot$ models.
4. Y_e of the ejecta has a broad mass distribution between ≈ 0.05 and ≈ 0.5 irrespective of the EOS and mass ratios. This property is well-suited for producing a variety of r-process heavy elements as illustrated in Refs. [16, 17].
5. The neutrino irradiation effect to the dynamical ejecta, which is clearly found for the DD2 models, becomes weak as the binary asymmetry degree increases. The reason for this is that binary asymmetry reduces the shock heating efficiency at the onset of the merger, and as a result, the temperature of the remnant MNS is decreased, reducing the luminosity of the neutrino emission from the MNS.

In our previous paper [12], we found for the equal-mass binary merger that the total ejecta mass is larger for softer EOS. It exceeds $0.01M_\odot$ only for the case that $R_{1.35} \lesssim 12 \text{ km}$ and it is of the order $10^{-3}M_\odot$ for $R_{1.35} > 13 \text{ km}$. For the case that the ejecta mass might be of the order $10^{-3}M_\odot$, it would be too small to explain the total mass of r-process heavy elements (the so-called second and third-peaks elements) in our galaxy, unless

the galactic merger rate of binary neutron stars is unexpectedly high [44] or some other ejection mechanisms such as the disk wind are present. Our present simulations show that the ejecta mass can be increased in the presence of an appreciable mass asymmetry of the binary systems even for the case that $R_{1.35} = 13.2$ km. This suggests that even if the EOS is not very soft, the observed total mass of the r-process heavy elements in our galaxy may be explained in the presence of a substantial fraction of the asymmetric merger events. Here, we stress that even from such asymmetric systems, neutron-rich matter with a variety of Y_e could be ejected.

Nevertheless, if a large fraction of the asymmetric binary merger has a mass ratio of $q \lesssim 0.9$, the averaged value of Y_e would be small $\lesssim 0.2$ even if the EOS is soft. In such case, although a substantial amount of the heavy r-process elements around the second and third peaks could be produced, the light elements around the first peak would not be significantly produced [16, 17]. If this scenario is the case, we have to rely on other components such as disk-wind components [35, 37], which can be produced in the merger remnant for a time scale longer than the dynamical one.

As we mentioned above, the r-process elements are likely to be produced in the neutron-rich ejecta. Because most of the produced r-elements are unstable, they subsequently decay and the released energy will be the source for an electromagnetic signal, in particular in the near-infrared optical band [9, 10]. Our present study indicates that irrespective of the EOS and mass ratios, the ejecta mass is larger than $10^{-3}M_{\odot}$. Under this condition, the expected observed magnitude in the near-infrared optical bands is smaller than 24 magnitude for an event at 100 Mpc from the earth. Such an event can be observed by Hyper-Suprime Cam (HSC) of the Subaru telescope with one-minute-duration observation [45]. Since HSC (in operation now) can simultaneously observe a field of ≈ 1.75 deg², a wide field of ~ 100 deg² can be surveyed in one night by it. Even if the position determination by gravitational-wave detectors is not very good (e.g., Ref. [46]), this wide-field observation will enable us to find a counterpart of the gravitational-wave events. These facts indicate that this radio-actively pow-

ered electromagnetic signal is the promising electromagnetic counterpart of binary-neutron-star mergers even for the gravitational-wave observation with a small number of detectors (by which the accuracy of the position determination is not very high).

Light curves for this emission have been calculated for the dynamical ejecta [9, 10], based on the numerical results for it. Only in the presence of the dynamical ejecta, the luminosity simply decreases with time in a power-law manner after the peak luminosity is reached in 1–10 days after the merger (the peak time depends on the wave length). Here, in the presence of disk-wind components, we will have two different types of the sources and hence the electromagnetic signals from the ejecta will be significantly modified [47].

For the observation of the electromagnetic counterparts, we need a reliable theoretical prediction for the light curves. This is in particular the case for searching the electromagnetic counterparts of short duration. For this issue, we have to take into account all the possible components other than the dynamical ejecta like the disk-wind components. We plan to explore this issue in the subsequent work.

ACKNOWLEDGMENTS

We are grateful to M. Hempel for providing the EOS table data and to M. Tanaka for helpful discussion on electromagnetic-counterpart observation. Numerical computations were performed on the supercomputer K at AICS, XC30 at CfCA of NAOJ, FX10 at Information Technology Center of Tokyo University, and SR16000 and XC30 at YITP of Kyoto University. This work was supported by Grant-in-Aid for Scientific Research (24244028, 25103510, 25105508, 24740163, 26400267, 15K05077, 15H06857, 15H00783, 15H00836), for Scientific Research on Innovative Area (24103001) of Japanese MEXT/JSPS, and by HPCI Strategic Program of Japanese MEXT (project No. hpci140211 and hpci150225). Kyutoku was supported by the RIKEN iTHES project.

-
- [1] J. Abadie *et al.* Nucl. Instrum. Meth. A **624**, 223 (2010); T. Accadia *et al.* Class. Quant. Grav. **28**, 025005 (2011) [Erratum-ibid. **28**, 079501 (2011)]; K. Kuroda, Class. Quant. Grav. **27**, 084004 (2010).
 - [2] B. P. Abbott *et al.*, Phys. Rev. Lett. **116**, 061102 (2016).
 - [3] J. Abadie *et al.* (The LIGO Scientific Collaboration and Virgo Collaboration), Class. Quantum Grav. **27**, 173001 (2010).
 - [4] M. Dominik, E. Berti, R. O’Shaughnessy, I. Mandel, K. Belczynski, C. Fryer, D. Holz, T. Bulik, and F. Pannarale, Astrophys. J. **806**, 263 (2015).
 - [5] C. Kim, B. B. P. Perera, and M. A. McLaughlin, Mon. Not. R. Astro. Soc. **448**, 928 (2015).
 - [6] J. M. Lattimer, & D. N. Schramm, Astrophys. J. **192**, L145 (1974).
 - [7] C. Freiburghaus, S. Rosswog, and F.-K. Thielemann, Astrophys. J. **525**, L121 (1998). S. Rosswog, M. Liebendorfer, F.-K. Thielemann, M. B. Davies, W. Benz, and T. Piran, Astron. Astrophys. **341** 499 (1999); S. Rosswog, M.B. Davies, F.-K. Thielemann, and T. Piran, Astron. Astrophys. **360** 171 (2000).
 - [8] L. -X. Li and B. Paczynski, Astrophys. J. **507**, L59 (1998).

- [9] D. Kasen, N. R. Badnell, J. Barnes, *Astrophys. J.* **774**, 25 (2013); J. Barnes and D. Kasen, *Astrophys. J.* **775**, 18 (2013).
- [10] M. Tanaka and K. Hotokezaka, *Astrophys. J.* **775**, 113 (2013).
- [11] N. R. Tanvir, A. J. Levan, A. S. Fruchter, J. Hjorth, R. A. Hounsell, K. Wiersema, & R. L. Tunnicliffe, *Nature*, **500**, 547 (2013); E. Berger, W. Fong, & R. Chornock, *Astrophys. J.* **774**, L23 (2013).
- [12] Y. Sekiguchi, K. Kiuchi, K. Kyutoku, and M. Shibata, *Phys. Rev. D* **91**, 064059 (2015).
- [13] C. Palenzuela, S.L. Liebling, D. Neilsen, L. Lehner, O.L. Caballero, E. O'Connor, and M. Anderson, *Phys. Rev. D* **92**, 044045 (2015); L. Lehner, S. L. Liebling, C. Palenzuela, O. L. Caballero, E. O'Connor, M. Anderson, and D. Neilsen, *ArXiv*: 1603.00501.
- [14] F. Foucart, R. Haas, M. D. Duez, E. O'Connor, C. D. Ott, L. Roberts, L. E. Kidder, J. Lippuner, H. P. Pfeiffer, and M. A. Scheel, *Phys. Rev. D* **93**, 044019 (2016).
- [15] S. Bernuzzi, D. Radice, C. D. Ott, L. F. Roberts, P. Moesta, and F. Galeazzi, *arXiv*:1512.06397 [gr-qc].
- [16] D. Radice, F. Galeazzi, J. Lippuner, L. F. Roberts, C. D. Ott, and L. Rezzolla, *arXiv*: 1601.02426 (2016).
- [17] S. Wanajo, Y. Sekiguchi, N. Nishimura, K. Kiuchi, K. Kyutoku, and M. Shibata, *Astrophys. J. Lett.* **789**, L39 (2014).
- [18] A. Steiner, M. Hempel, and T. Fischer, *Astrophys. J.* **774**, 17 (2013).
- [19] S. Banik, M. Hempel, and D. Bandyopadhyay, *Astrophys. J. Suppl. Ser.* **214**, 22 (2014).
- [20] M. Shibata and T. Nakamura, *Phys. Rev. D* **52**, 5428(1995); T. W. Baumgarte and S. L. Shapiro, *Phys. Rev. D* **59**, 024007(1998); M. Campanelli, C. O. Lousto, P. Marronetti, and Y. Zlochower, *Phys. Rev. Lett.* **96**, 111101 (2006); J. G. Baker, J. Centrella, D.-I. Choi, M. Koppitz, and J. van Meter, *Phys. Rev. Lett.* **96**, 111102 (2006).
- [21] Y. Sekiguchi, K. Kiuchi, K. Kyutoku, and M. Shibata, *Phys. Rev. Lett.* **107**, 051102; *ibid.*, **107**, 211101 (2011)
- [22] Y. Sekiguchi, K. Kiuchi, K. Kyutoku, and M. Shibata, *Prog. Theor. Exp. Phys.* **01**, A304 (2012).
- [23] K. S. Thorne, *Mon. Not. R. Astro. Soc.* **194**, 439 (1981).
- [24] M. Shibata, K. Kiuchi, Y. Sekiguchi, and Y. Suwa, *Prog. Theor. Phys.* **125**, 1255 (2011).
- [25] P. Demorest, T. Pennucci, S. Ransom, M. Roberts and J. Hessels, *Nature* **467**, 1081 (2010); J. Antoniadis, P. C. C. Freire, N. Wex, T. M. Tauris, R. S. Lynch, M. H. van Kerkwijk, M. Kramer and C. Bassa *et al.*, *Science* **340**, 6131 (2013).
- [26] E.g., D. R. Lorimer, *Living. Rev. Relativ.* **11**, 8 (2008).
- [27] K. Hotokezaka, K. Kiuchi, K. Kyutoku, T. Muranushi, Y. Sekiguchi, M. Shibata and K. Taniguchi, *Phys. Rev. D* **88**, 044026 (2013).
- [28] M. Shibata, K. Taniguchi, and K. Uryū, *Phys. Rev. D* **71**, 084021 (2005); M. Shibata and K. Taniguchi, *Phys. Rev. D* **73**, 064027 (2006).
- [29] T. W. Baumgarte, S. L. Shapiro, and M. Shiabta, *Astrophys. J. Lett.* **528**, L28 (2000).
- [30] M. Shibata, *Numerical Relativity* (World Scientific, 2016).
- [31] K. Kiuchi, K. Kyutoku, Y. Sekiguchi, M. Shibata, and T. Wada, *Phys. Rev. D* **90**, 041502 (2014); K. Kiuchi, Y. Sekiguchi, K. Kyutoku, M. Shibata, K. Taniguchi, and T. Wada, *Phys. Rev. D* **92**, 064034 (2015).
- [32] K. Hotokezaka, K. Kiuchi, K. Kyutoku, H. Okawa, Y. Sekiguchi, M. Shibata, and K. Taniguchi, *Phys. Rev. D* **87**, 024001 (2013).
- [33] A. Bauswein, S. Goriely, H.-T. Janka, *Astrophys. J.* **773**, 78 (2013)
- [34] L. Dessart, C. D. Ott, A. Burrows, S. Rosswog, and E. Livne, *Astrophys. J.* **690**, 1681 (2009).
- [35] R. Fernández and B. Metzger, *Mon. Not. Royal Astron. Soc.* **435**, 502 (2013)
- [36] A. Perego, S. Rosswog, R. Cabezon, O. Korobkin, R. Kaeppli, A. Arcones, M. Liebendoerfer, *Mon. Not. Royal Astron. Soc.* **443**, 3134 (2014).
- [37] O. Just, A. Bauswein, R. A. Pulpillo, S. Goriely, and H.-Th. Janka *Mon. Not. Royal Astron. Soc.* **448**, 541 (2015).
- [38] D. Martin, A. Perego, A. Arcones, F.-K. Thielemann, O. Korobkin, and S. Rosswog, *Astrophys. J.* **813**, 2 (2015).
- [39] Y.-Z. Qian and S. E. Woosley, *Astrophys. J.* **471**, 331 (1996).
- [40] L. Zalamea and A. M. Beloborodov, *Mon. Not. R. Astro. Soc.* **410**, 2302 (2011).
- [41] O. Just, M. Obergaulinger, H.-T. Janka, A. Bauswein, and N. Schwarz, *Astrophys. J. Lett.* **816**, L30 (2016).
- [42] J. Cooperstein, L. J. van den Horn, and E. Baron, *Astrophys. J. Lett.* **321**, L129 (1987); H.-Th. Janka, *Astron. Astrophys.* **244**, 378 (1991).
- [43] H. Nagakura, K. Hotokezaka, Y. Sekiguchi, M. Shibata, and K. Ioka, *Astrophys. J. Lett.* **784**, L28 (2014).
- [44] K. Hotokezaka, T. Piran, and M. Paul, *Nature Physics* **11**, 1042 (2015)
- [45] M. Tanaka, private communication.
- [46] S. Nissanke, M. M. Kasliwal, and A. Georgieva, *Astrophys. J.* **767**, 124 (2013); M. M. Kasliwal and S. Nissanke, *Astrophys. J.* **789**, L5 (2014).
- [47] D. Kasen, R. Fernández, B. D. Metzger, *Mon. Not. R. Astro. Soc.* **450**, 1777 (2015).